

Compositional Simulation of CO₂ Huff 'n' Puff in Eagle Ford Tight Oil Reservoirs With CO₂ Molecular Diffusion, Nanopore Confinement, and Complex Natural Fractures

Wei Yu, Texas A&M University and University of Texas at Austin; Yuan Zhang, China University of Geosciences, Beijing; Abdoljalil Varavei, Kamy Sepehrnouri, and Tongwei Zhang, University of Texas at Austin; Kan Wu, Texas A&M University; and Jijun Miao, SimTech

Summary

Although numerous studies proved the potential of carbon dioxide (CO₂) huff 'n' puff, relatively few models exist to comprehensively and efficiently simulate CO₂ huff 'n' puff in a way that considers the effects of molecular diffusion, nanopore confinement, and complex fractures for CO₂. The objective of this study was to introduce a numerical compositional model with an embedded-discrete-fracture-model (EDFM) method to simulate this process in an actual Eagle Ford tight oil well. Through nonneighboring connections (NNCs), the EDFM method can properly and efficiently handle any complex fracture geometries. We built a 3D reservoir model with six fluid pseudocomponents. We performed history-matching with measured flow rates and bottomhole pressure (BHP). Good agreements between field data, EDFM, and local grid refinement (LGR) were achieved. However, the EDFM method performed faster than the LGR method. After that, we evaluated the CO₂-enhanced-oil-recovery (EOR) effectiveness for molecular diffusion and nanopore confinement effects. The traditional phase equilibrium calculation was modified to calculate the critical fluid properties with nanopore confinement. The simulation results showed that the CO₂ EOR with larger diffusion coefficients performed better than the primary production. In addition, both effects were favorable for the CO₂ huff 'n' puff effectiveness. The relative increase of cumulative oil production after 20 years was approximately 12% for this well. Furthermore, when considering complex natural fractures, the relative increase of cumulative oil production was approximately 8%. This study provided critical insights into a better understanding of the impacts of CO₂ molecular diffusion, nanopore confinement, and complex natural fractures on well performance during the CO₂-EOR process in tight oil reservoirs.

Introduction

Multiwell pads with multistage hydraulic fracturing were widely used in the economic development of tight oil reservoirs, such as Eagle Ford, Bakken, and Permian. Although a large contact area was created between the reservoir and fractures, which significantly increased the flow path of hydrocarbon flow, the decline curves of tight oil reservoirs were steeper and the primary oil recovery factor remained very low because of low permeability. Hence, vast amounts of oil remained in tight rocks, making it important to investigate EOR methods in unconventional reservoirs.

Recently, the approach of CO₂ EOR in tight oil reservoirs has received much attention (Kurtoglu et al. 2013; Song and Yang 2013; Adekunle and Hoffman 2014). Although CO₂ EOR has been well-studied and -understood in conventional oil reservoirs, it is still a new subject in unconventional oil reservoirs. Hawthorne et al. (2013) described five conceptual steps for CO₂ injection in tight oil reservoirs: (1) CO₂ flows into and through the fractures, (2) unfractured rock matrix is exposed to CO₂ at fracture surfaces, (3) CO₂ permeates the rock driven by pressure, carrying some hydrocarbon inward; however, the oil is also swelling and extruding some oil out of the pores, (4) oil migrates to the bulk CO₂ in the fractures by means of swelling and reduced viscosity, and (5) as the CO₂ pressure gradient gets smaller, oil production is slowly driven by concentration-gradient diffusion from pores into the bulk CO₂ in the fractures. The physical mechanisms for CO₂ EOR in fractured reservoirs mainly involve viscous forces, gravity drainage, and molecular diffusion (Hoteit 2013). However, molecular diffusion plays a more important role in a tight oil reservoir with low permeability than viscous forces and gravity drainage (Hoteit and Firoozabadi 2006).

Although many simulation studies were conducted to evaluate CO₂ EOR in tight oil reservoirs (Shoaib and Hoffman 2009; Wang et al. 2010; Ren et al. 2011; Chen et al. 2014), the mechanism of CO₂ molecular diffusion on CO₂-EOR effectiveness is not well-examined. Yu et al. (2014) performed a series of simulation studies for CO₂ EOR in the Bakken Formation and concluded that the CO₂ molecular diffusivity was very important for CO₂ injection in tight oil reservoirs, which should be correctly captured in a numerical reservoir simulation. In addition, Yu et al. (2015) simulated and compared the contribution of CO₂ molecular diffusion to incremental oil recovery in the Bakken tight oil reservoir using one perforation stage with four biwing hydraulic fractures. They found that, after 10 years, the incremental oil recovery factor was approximately 2.9% and -1.2%, with and without consideration of CO₂ molecular diffusion; without considering this physical mechanism, most injected CO₂ molecules concentrated around fractures and were difficult to diffuse into the shale matrix, resulting in a negative incremental oil recovery factor.

Another mechanism of nanopore confinement should also be considered for an accurate simulation of CO₂ EOR in unconventional reservoirs because nanopores in unconventional reservoirs often lead to high capillary pressure, which significantly impacts phase behavior and fluid properties (Zhang et al. 2016; Zhang et al. 2017b, 2017c). A new equation of state (EOS) was needed to calculate the phase behavior when considering the capillary pressure effect (Brusilovsky 1992). Although there are many compositional-model

developments reported in the literature that demonstrate the importance of implementing the nanopore confinement effect (Nojabaei et al. 2014; Rezaveisi et al. 2015; Sandoval et al. 2015), very few studies quantitatively evaluated CO₂ EOR in unconventional reservoirs. The impacts of physical mechanisms, such as molecular diffusion and nanopore confinement, on CO₂ EOR in tight oil reservoirs have not yet been fully investigated and clearly understood.

In addition to complex physical mechanisms, complex fracture geometries should also be accounted for when simulating CO₂ EOR in unconventional reservoirs. Complex fracture geometries are often generated during the hydraulic-fracturing process, especially in the presence of large amounts of natural fractures (Wu et al. 2012; Cipolla and Wallace 2014; Wu and Olson 2016). Such complex fracture patterns require an easy and fast reservoir-simulation model to quantify their impact on well performance during CO₂-EOR processes. The existing discrete fracture models that use unstructured gridding with LGR can better model complex fractures (Mirzaei and Cipolla 2012; Sandve et al. 2012; Hui et al. 2013). However, complicated gridding issues and an expensive computational cost are often encountered. To overcome these issues, a state-of-the-art EDFM was developed (Li and Lee 2008; Moynfar et al. 2014; de Araujo Cavalcante Filho et al. 2015; Shakiba and Sepehrnoori 2015; Yu et al. 2018). The EDFM method was reported to easily and efficiently model complex fracture geometries (Xu 2015; Zuloaga-Molero et al. 2016; Xu et al. 2017a, 2017b; Zhang et al. 2017d).

In this study, we focused on a compositional simulation of the CO₂ huff 'n' puff process with typical reservoir and fluid properties from the Eagle Ford tight oil reservoir. Six pseudocomponents were assigned to the Eagle Ford tight oil composition. We performed history matching with an actual Eagle Ford tight oil well using the traditional LGR approach and the EDFM method. After the history-matching period, we continued to perform the simulation with five cycles of CO₂ huff 'n' puff (one cycle represented 90 days of CO₂ injection, 90 days of CO₂ soaking, and 720 days of back production). We investigated the impact of different mechanisms of CO₂ molecular diffusion and nanopore confinement and of complex natural fractures on the effectiveness of CO₂ huff 'n' puff in detail. Our study provides a better understanding of the influences of key physical mechanisms and complex natural fractures on CO₂ EOR in tight oil reservoirs.

Modeling Nanopore-Confinement Effect on Phase Behavior

The fluid properties and phase behavior were altered when the nanopore radius was 10 nm or less in shale reservoirs because of the strong interactions between surface walls and fluid molecules, especially the critical temperatures and pressures (Diaz Campos et al. 2009; Devegowda et al. 2012; Zhang et al. 2016). The correlations for the shifts in these critical properties are described as follows:

$$\Delta T_c^* = \frac{T_{cb} - T_{cp}}{T_{cb}} = 0.9409 \frac{\sigma_{LJ}}{r_p} - 0.2415 \left(\frac{\sigma_{LJ}}{r_p} \right)^2, \quad \dots \dots \dots (1)$$

$$\Delta P_c^* = \frac{P_{cb} - P_{cp}}{P_{cb}} = 0.9409 \frac{\sigma_{LJ}}{r_p} - 0.2415 \left(\frac{\sigma_{LJ}}{r_p} \right)^2, \quad \dots \dots \dots (2)$$

$$\sigma_{LJ} = 0.244 \sqrt[3]{\frac{T_{cb}}{P_{cb}}}, \quad \dots \dots \dots (3)$$

where r_p is the pore-throat radius; ΔT_c^* and ΔP_c^* are the relative critical temperature and pressure shift because of nanopore confinement, respectively; T_{cb} is the bulk critical temperature; T_{cp} is the pore critical temperature; P_{cb} is the bulk critical pressure; P_{cp} is the pore critical pressure; and σ_{LJ} is the Lennard-Jones size parameter. The critical properties for each component were reported by Reid et al. (1987). In our previous study, we described the phase equilibrium calculation (Zhang et al. 2016; Zhang et al. 2017b, 2017c). The fugacity of the components in the liquid and vapor phases were equal at equilibrium, which can be expressed by

$$f_L^i(T, P_L, x_i) = f_V^i(T, P_V, y_i), i = 1, \dots, N_c, \quad \dots \dots \dots (4)$$

where f_L^i and f_V^i are the fugacity of the component i in the liquid and vapor phases, respectively; T is the reservoir temperature; and P_L and P_V represent the pressures in the liquid and vapor phases, respectively.

The following mass-balance equation and the Rachford-Rice equation (Rachford and Rice 1952) were used in this study:

$$\sum_{i=1}^{N_c} x_i = \sum_{i=1}^{N_c} y_i = 1, \quad \dots \dots \dots (5)$$

$$Fz_i = x_iL + y_iV, i = 1, \dots, N_c, \quad \dots \dots \dots (6)$$

where F is the number of moles of original fluid feed; L and V are the number of moles of liquid and vapor phases, respectively; z_i is the overall mole fraction of component i ; x_i and y_i are the mole fractions of component i in the liquid and vapor phases, respectively; and N_c is the number of components.

Capillary pressure refers to the difference between vapor and liquid phases. We used the following Young-Laplace equation (Adamson 1990) to calculate the capillary pressure:

$$P_V - P_L = P_{cap}, \quad \dots \dots \dots (7)$$

$$P_{cap} = \frac{2\sigma \cos \theta}{r_p}, \quad \dots \dots \dots (8)$$

where P_{cap} is the capillary pressure, θ is the contact angle, and σ is the interfacial tension at the interface between the vapor and liquid phases, which was calculated using the parachor model (Adamson 1990):

$$\sigma = \left\{ \sum_{i=1}^{N_c} (\bar{\rho}_L [P]_i x_i - \bar{\rho}_V [P]_i y_i) \right\}^v, \quad \dots \dots \dots (9)$$

where $\bar{\rho}_L$ and $\bar{\rho}_V$ are densities of the bulk liquid and vapor phases, respectively; v is the scaling exponent (we used 4.0 in this study); and $[P]_i$ is the parachor of component i in the liquid or gas phase. The parachor of pure component was reported by Reid et al. (1987).

In this study, the Peng-Robinson EOS (Peng and Robinson 1976) was used in the phase equilibrium calculation:

$$P = \frac{RT}{V_m - b} - \frac{a\alpha}{V_m^2 + 2bV_m - b^2}, \quad \dots \dots \dots (10)$$

where V_m is the mole volume of component i , R is the universal gas constant, and a and b are the parameters calculated using van der Waals mixing rules. Considering the difference between vapor and liquid pressures, Eq. 10 was modified for liquid and vapor phases, respectively:

$$(Z_L)^3 - (1 - B_L)(Z_L)^2 + [A_L - 2B_L - 3(B_L)^2]Z_L - [A_L B_L - (B_L)^2 - (B_L)^3] = 0, \quad \dots \dots \dots (11)$$

$$(Z_V)^3 - (1 - B_V)(Z_V)^2 + [A_V - 2B_V - 3(B_V)^2]Z_V - [A_V B_V - (B_V)^2 - (B_V)^3] = 0, \quad \dots \dots \dots (12)$$

where $A_L = \frac{a_L \alpha P_L}{R^2 T^2}$, $B_L = \frac{b_L P_L}{RT}$, $A_V = \frac{a_V \alpha P_V}{R^2 T^2}$, $B_V = \frac{b_V P_V}{RT}$, and Z_L and Z_V are the compressibility of liquid and vapor phases, respectively. The root of the compressibility factors for liquid and vapor phases were determined by satisfying the criteria of Gibbs free energy for liquid and vapor. The additional calculation procedure can be found in Zhang et al. (2016).

The following equations were used to calculate the fugacity coefficients of liquid and vapor phases:

$$\ln \phi_L^i = \frac{b_{iL}}{b_L} (Z_L - 1) - \ln(Z_L - B_L) - \frac{A_L}{2\sqrt{2}B_L} \left[\frac{2 \sum_{j=1}^{N_c} x_{jL} (1 - k_{ij}) \sqrt{a_{iL} a_{jL}}}{a_L} - \frac{b_{iL}}{b_L} \right] \ln \left[\frac{Z_L + (\sqrt{2} + 1)B_L}{Z_L - (\sqrt{2} - 1)B_L} \right] \quad \dots \dots \dots (13)$$

$$\ln \phi_V^i = \frac{b_{iV}}{b_V} (Z_V - 1) - \ln(Z_V - B_V) - \frac{A_V}{2\sqrt{2}B_V} \left[\frac{2 \sum_{j=1}^{N_c} x_{jV} (1 - k_{ij}) \sqrt{a_{iV} a_{jV}}}{a_V} - \frac{b_{iV}}{b_V} \right] \ln \left[\frac{Z_V + (\sqrt{2} + 1)B_V}{Z_V - (\sqrt{2} - 1)B_V} \right] \quad \dots \dots \dots (14)$$

A detailed flow chart is shown in **Fig. 1**.

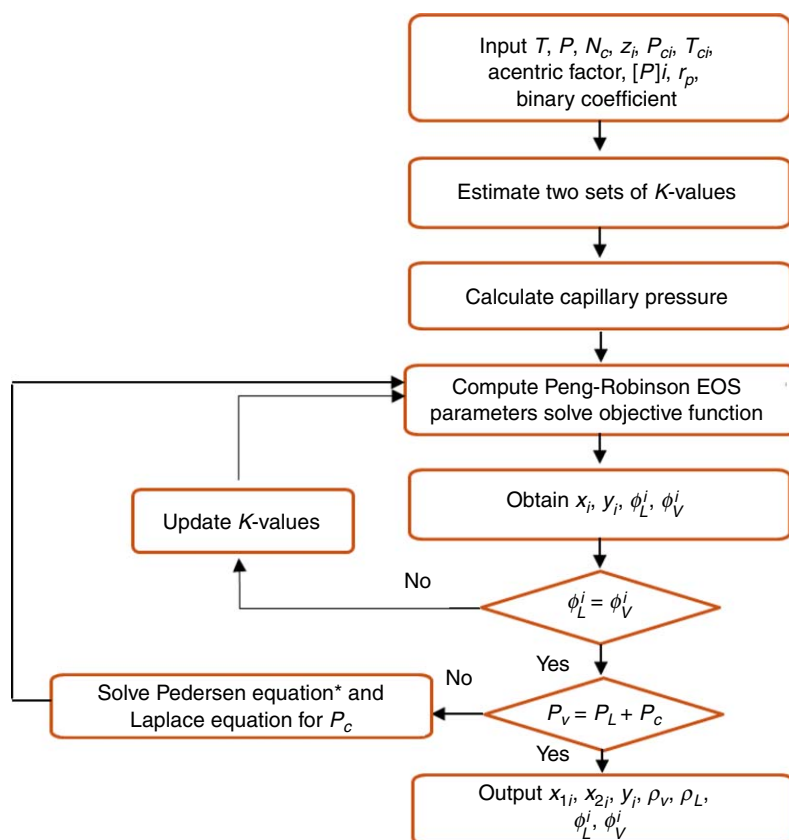


Fig. 1—Flow chart for phase equilibrium calculation considering the capillary pressure effect resulting from nanopore confinement (modified from Zhang et al. 2016). *Pedersen and Christensen (2007).

Modeling Complex Fractures Using EDFM

The EDFM method is used to model complex fracture geometries using structured gridding (Moinfar et al. 2014; Xu 2015). In this method, complex fractures are discretized into fracture segments on the basis of the interaction between fracture geometry and structured matrix gridblock boundaries. Consequently, some virtual cells are created to represent these fracture segments. The fluid transport among the fractures, the matrix, and the well can be simulated inside reservoir simulators using NNCs and an effective wellbore index.

In total, four types of NNC pairs need to be considered: fluid flow between matrix cells and fracture segments inside them, fluid flow between fracture segments within an individual fracture, fluid flow between intersecting fracture segments within different fractures, and fluid flow between fracture segments and the wellbore. The following general equation was used to calculate the transmissibility factor for the first three types of connections:

$$T_{NNC} = \frac{k_{NNC} A_{NNC}}{d_{NNC}}, \quad (15)$$

where k_{NNC} represents permeability associated with different connections with (1) k_{NNC} being the matrix permeability for the connection between matrix and fracture segments and (2) k_{NNC} being the average fracture permeability for the connection between fracture segments; A_{NNC} is the contact area between the NNC pair; and d_{NNC} is the distance between the NNC pair with (1) d_{NNC} being an average distance from the matrix gridblock to the fracture plane for the connection between matrix and fracture segments and (2) d_{NNC} being the summation of the distances measured from the centroids of the fracture segments to the common line between different fracture segments for the connection between fracture segments.

The following modified Peaceman's model was used to calculate the effective wellbore index for the connection between fracture segments and wellbore:

$$W_{If} = \frac{2\pi k_f w_f}{\ln(r_e/r_w)}, \quad (16)$$

$$r_e = 0.14 \sqrt{L_{fs}^2 + W_{fs}^2}, \quad (17)$$

where w_f represents the fracture width, k_f is the fracture permeability, L_{fs} is the fracture-segment length, and W_{fs} is the fracture-segment height. Additional details about the calculation were reported by Xu et al. (2017a).

History Matching With an Eagle Ford Tight Oil Well

In order to investigate CO₂-EOR effectiveness in tight oil reservoirs, an actual well with available production data for 583 days from Eagle Ford was selected to perform history matching. The well was stimulated with 19 perforation stages with four clusters per stage. In this study, it was assumed that there were 76 effective hydraulic fractures. More details about the well completion can be found by Simpson et al. (2016). Because the detailed fluid characterization data for this Eagle Ford well were not available, six pseudocomponents were assigned in this study: CO₂, N₂, C₁, C₂–C₅, C₆–C₁₀, and C₁₁₊. The corresponding molar fractions were 0.01183, 0.00161, 0.11541, 0.26438, 0.38089, and 0.22588, respectively. **Tables 1 and 2** list the critical properties of these pseudocomponents and their binary interaction parameters, which were used for phase behavior calculation. In addition, CO₂ solubility in water was not considered in the simulations. The oil properties were determined for this well using the Peng-Robinson EOS and flash calculations under a reservoir temperature of 270°F without considering the capillary pressure effect: oil gravity was 40 °API, gas/oil ratio was 1900 scf/STB, formation volume factor was 1.65 RB/STB, and the bubblepoint was 3,446 psi.

Component	Molar Fraction	Critical Pressure (atm)	Critical Temperature (K)	Critical Volume (L/mol)	Molar Weight (g/g mol)	Acentric Factor	Parachor Coefficient
CO ₂	0.01183	72.80	304.20	0.0940	44.01	0.2250	78.00
N ₂	0.00161	33.50	126.20	0.0895	28.01	0.0400	41.00
C ₁	0.11541	45.40	190.60	0.0990	16.04	0.0080	77.00
C ₂ –C ₅	0.26438	36.50	274.74	0.2293	52.02	0.1723	171.07
C ₆ –C ₁₀	0.38089	25.08	438.68	0.3943	103.01	0.2839	297.42
C ₁₁₊	0.22588	17.55	740.29	0.8870	267.15	0.6716	661.45

Table 1—Compositional data for the Peng-Robinson EOS in the Eagle Ford well.

Component	CO ₂	N ₂	C ₁	C ₂ –C ₅	C ₆ –C ₁₀	C ₁₁₊
CO ₂	0	0.0200	0.1030	0.1299	0.1500	0.1500
N ₂	0.0200	0	0.0310	0.0820	0.1200	0.1200
C ₁	0.1030	0.0310	0	0.0174	0.0462	0.1110
C ₂ –C ₅	0.1299	0.0820	0.0174	0	0.0073	0.0444
C ₆ –C ₁₀	0.1500	0.1200	0.0462	0.0073	0	0.0162
C ₁₁₊	0.1500	0.1200	0.1110	0.0444	0.0162	0

Table 2—Binary interaction parameters for oil components in the Eagle Ford well.

We built a 3D reservoir model with a horizontal well and multiple hydraulic fractures using a numerical reservoir simulator (CMG-GEM 2016). The model dimensions were 7,785 × 1,300 × 100 ft, which correspond to length, width, and height, respectively, as shown in **Fig. 2a**. Three layers were modeled with the middle layer fully penetrated by hydraulic fractures. There was no vertical heterogeneity, and the gravity effect was ignored. A horizontal well with a length of 6,913 ft was placed in the middle layer. First, the EDFM method was applied to model multiple biwing hydraulic fractures in the numerical reservoir simulator. A small portion of the third layer with multiple fractures is shown in **Fig. 2b**. It can be clearly seen that hydraulic fractures were directly embedded into the matrix grids. **Table 3** lists the basic reservoir and fracture properties used in the simulation. During the history-matching process, the measured

oil-flow rate was used as a constraint input. The measured gas-flow rate, water-flow rate, and BHP were considered as history-matching objectives. Fracture height, fracture half-length, fracture conductivity, water saturation inside stimulated reservoir volume, K_V/K_H , and relative permeability curves were the main tuning parameters for achieving good match results. The natural-fracture characterization data for this well were not available. In addition, the natural-fracture distribution was highly uncertain. Hence, the impact of natural fractures on history matching was not considered. Comparisons of well performance and BHP between actual data and model results are presented in **Fig. 3**, illustrating that reasonable agreements were obtained. The simulated pressure was higher than the field data during very early time and during the shutdown periods, possibly caused by higher fracture conductivity or effective permeability in the model. The determined relative permeability curves, such as water/oil relative permeability and liquid/gas relative permeability, are given in **Fig. 4**.

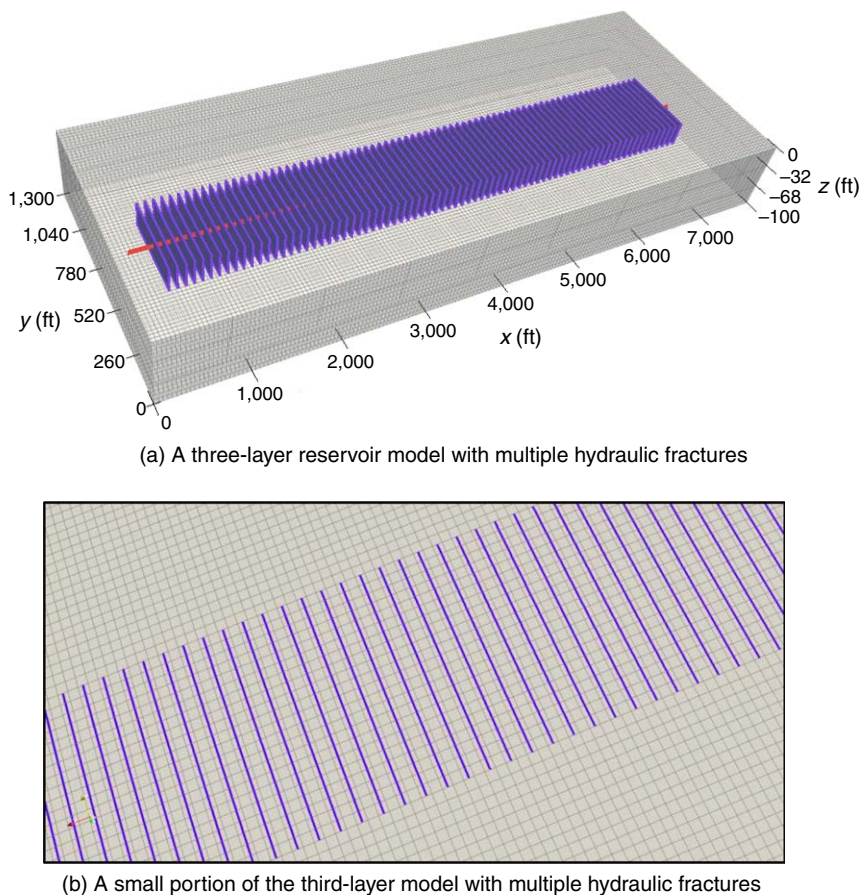


Fig. 2—A 3D reservoir model with a horizontal well and 76 biwing hydraulic fractures: (a) a three-layer reservoir model with multiple hydraulic fractures, (b) a small portion of the third-layer model with multiple hydraulic fractures.

Next, we compared well performance and pressure response between LGR and EDFM methods, as shown in **Fig. 5**. The LGR model for each matrix grid with hydraulic fracture was set at $7 \times 1 \times 1$ to fully capture the transient flow behavior of fluid transfer from the matrix to fractures, as shown in **Fig. 6**. The fracture aperture was 0.01 ft. The block size was 45×20 ft in the x - and y -direction. The block size was 32, 36, and 32 ft for three layers in the z -direction. The other inputs for the LGR model were the same as those in Table 3. Both EDFM and LGR models used the same solver and the same timestep. As shown in Fig. 5, agreement was achieved between LGR and EDFM. This might be because of the small matrix gridblock size used in the two models. **Fig. 7** compares the pressure distribution of the totaled three layers with the middle layer at the end of simulation between LGR and EDFM, illustrating that a good match was obtained. In addition, the ratio of central processing unit time between LGR and EDFM was approximately 1.5. The EDFM method offers easy setup for hydraulic fractures and efficient running for the model to perform history matching. Hence, the EDFM method was used for the following simulation studies.

Simulation of CO₂ Huff 'n' Puff in Eagle Ford

Effect of CO₂ Molecular Diffusion. After the history-matching period, we changed the producer of the horizontal well to a CO₂ injector and performed CO₂ huff 'n' puff simulation. Maximum for the CO₂-injection rate was set at 5,000 Mscf/D and the maximum BHP was set at 8,000 psi. After 90 days of CO₂ injection, the horizontal well was shut in and soaked for 90 days. Then, the well was put back into production for 720 days with a minimum BHP of 2,000 psi. Hence, the period of one cycle of CO₂ huff 'n' puff was 900 days. After one cycle of CO₂ huff 'n' puff simulation, another cycle began. In total, five cycles of CO₂ huff 'n' puff were assigned and simulated. The sensitivity analysis of CO₂-injection rate, injection time, soaking time, and cycle number was beyond the scope of this study. After that, the horizontal well was producing under the constraint of the minimum BHP of 2,000 psi for 2,216 days. A total simulation time of 7,300 days was considered. It should be mentioned that the impact of CO₂-injection rate, CO₂-injection time, CO₂-soaking time, and number of CO₂ huff 'n' puff cycles was not examined in this study, but will be investigated in detail in our future work.

Parameters	Value	Unit
Model dimension ($x \times y \times z$)	7,785 \times 1,300 \times 100	ft
Number of gridblocks ($x \times y \times z$)	173 \times 65 \times 3	—
Initial reservoir pressure	8,125	psi
Reservoir temperature	270	°F
Reservoir permeability	900	nd
Reservoir porosity	12%	—
Initial water saturation	17%	—
Total compressibility	1×10^{-6}	psi ⁻¹
Reservoir thickness	100	ft
Reservoir depth	11,109	ft
Well length	6,913	ft
Number of stages	19	—
Clusters per stage	4	—
Cluster spacing	90	ft
K_v/K_H (HM parameter)	0.06	—
Water saturation inside simulated reservoir volume (HM parameter)	33%	—
Fracture half-length (HM parameter)	210	ft
Fracture height (HM parameter)	36	ft
Fracture conductivity (HM parameter)	200	md-ft

Table 3—Basic reservoir and fracture properties used for history matching (HM parameter represents history-matching variables).

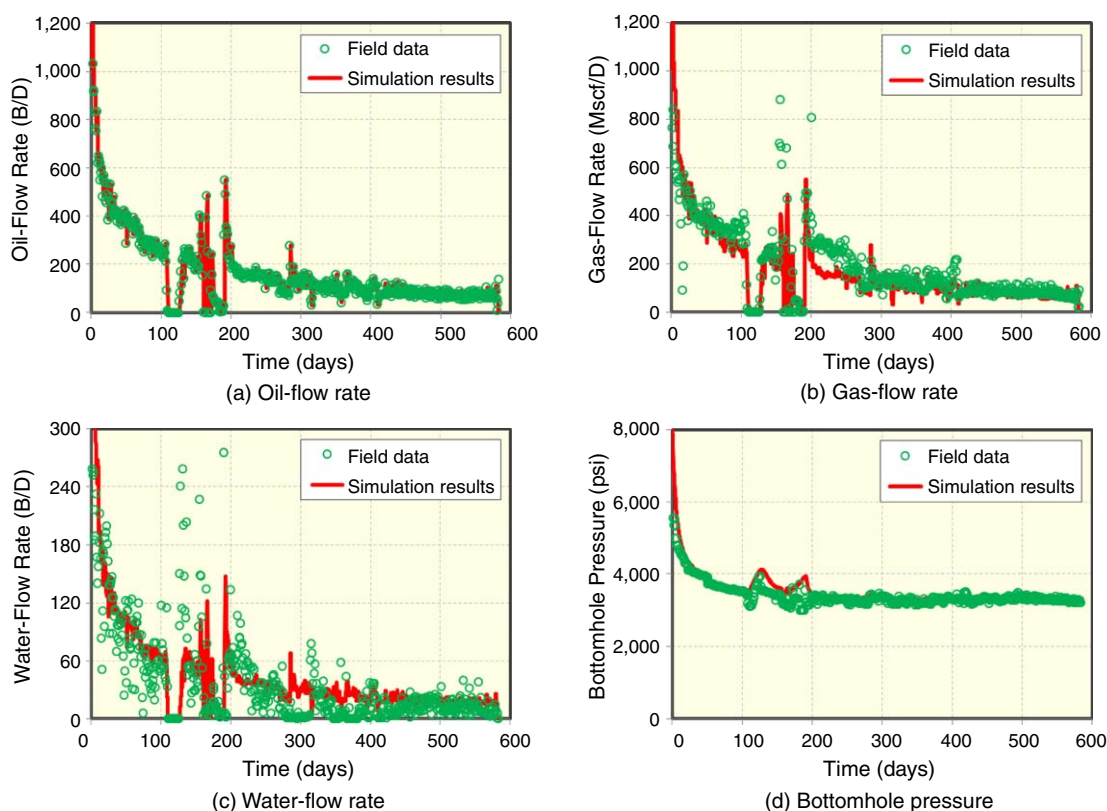


Fig. 3—Comparison of well performance and BHP between actual data and model results.

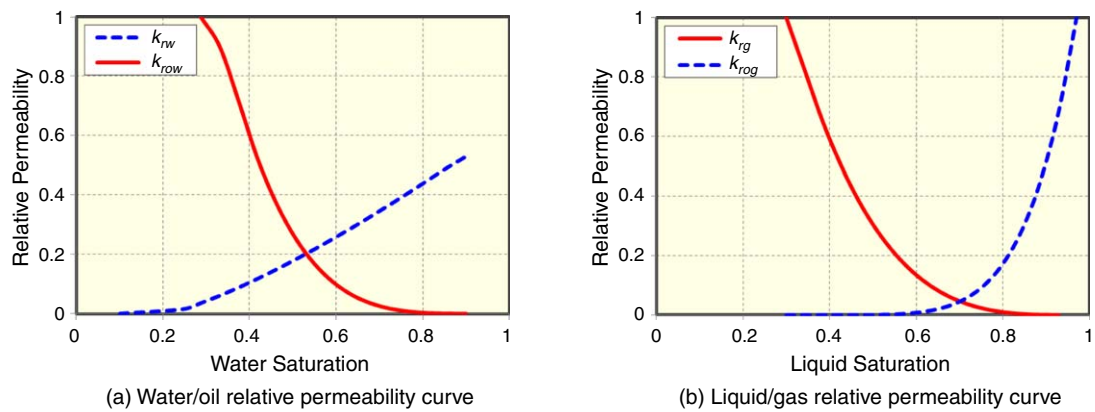


Fig. 4—Relative permeability curves based on the history matching in this study.

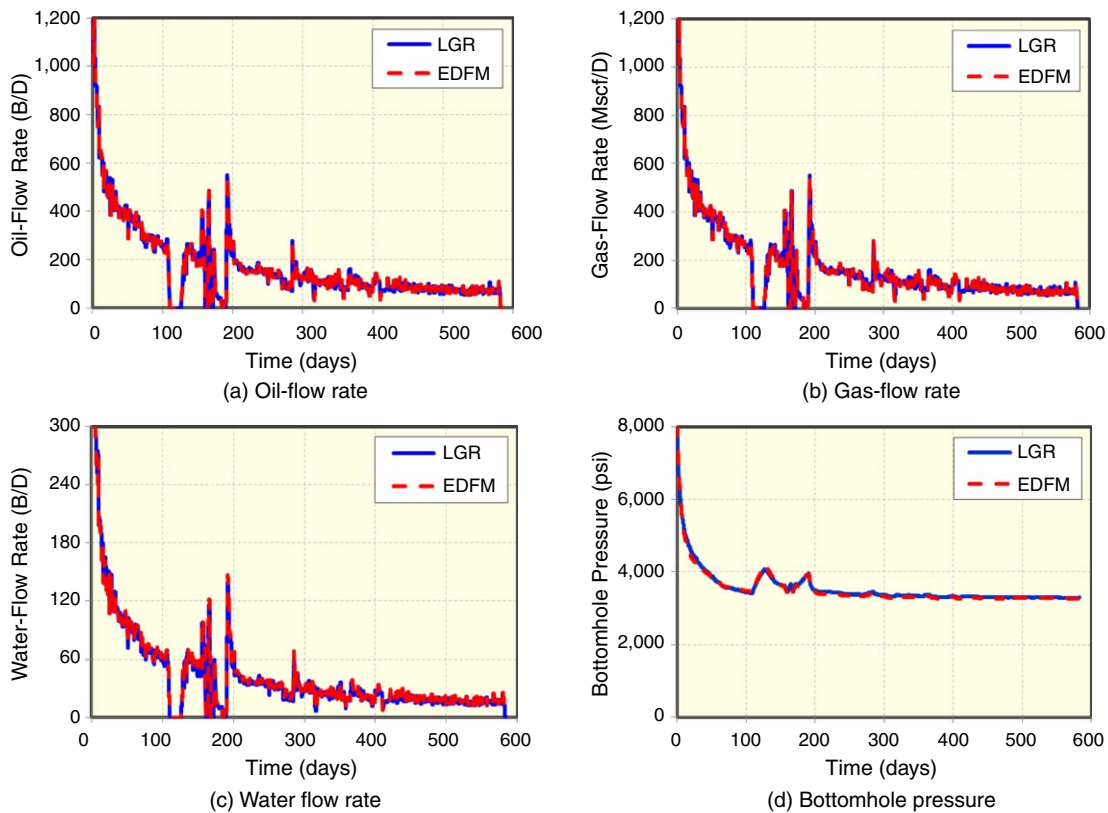


Fig. 5—Comparison of well performance and BHP between LGR and EDFM.

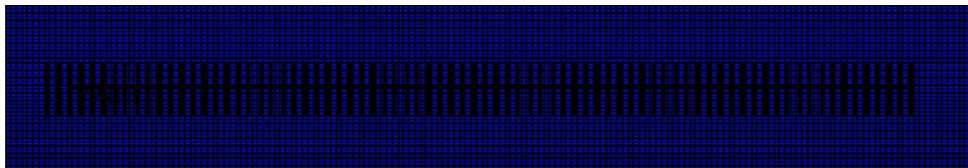


Fig. 6—The LGR model for the middle layer containing 76 biwing hydraulic fractures.

In order to investigate CO₂ huff 'n' puff effectiveness, the effect of CO₂ molecular diffusion was considered.

More details about the material-balance equation with the dispersion term and how molecular diffusion was considered in reservoir simulations can be found in Yu et al. (2015). The measured CO₂ diffusion coefficients in pentane, decane, and hexadecane at a temperature of 77°F and pressure up to 870 psi ranged from 1.80×10^{-5} to 7.59×10^{-5} cm²/s (Grogan et al. 1988). The range of measured CO₂ diffusion coefficients in decane at a temperature of 100°F and pressure up to 850 psi was approximately 1.97×10^{-5} to 1.26×10^{-4} cm²/s (Renner 1988). Kumar and Mittal (1999) stated that the CO₂ diffusion coefficients under the supercritical condition were 10 to 100 times those under the liquid condition. A range of CO₂ diffusion coefficient measured at 0.00001 to 0.01 cm²/s was investigated in this field

case study. During the CO₂ huff 'n' puff simulation, we only considered the CO₂ diffusion coefficient in the oil and gas phases. It was assumed that the diffusion coefficient in the liquid phase was the same as that used in the gas phase. The ratio of diffusion coefficient in different phases was beyond the scope of this study and needs further research. The diffusion coefficients of the other components were assumed to be zero.

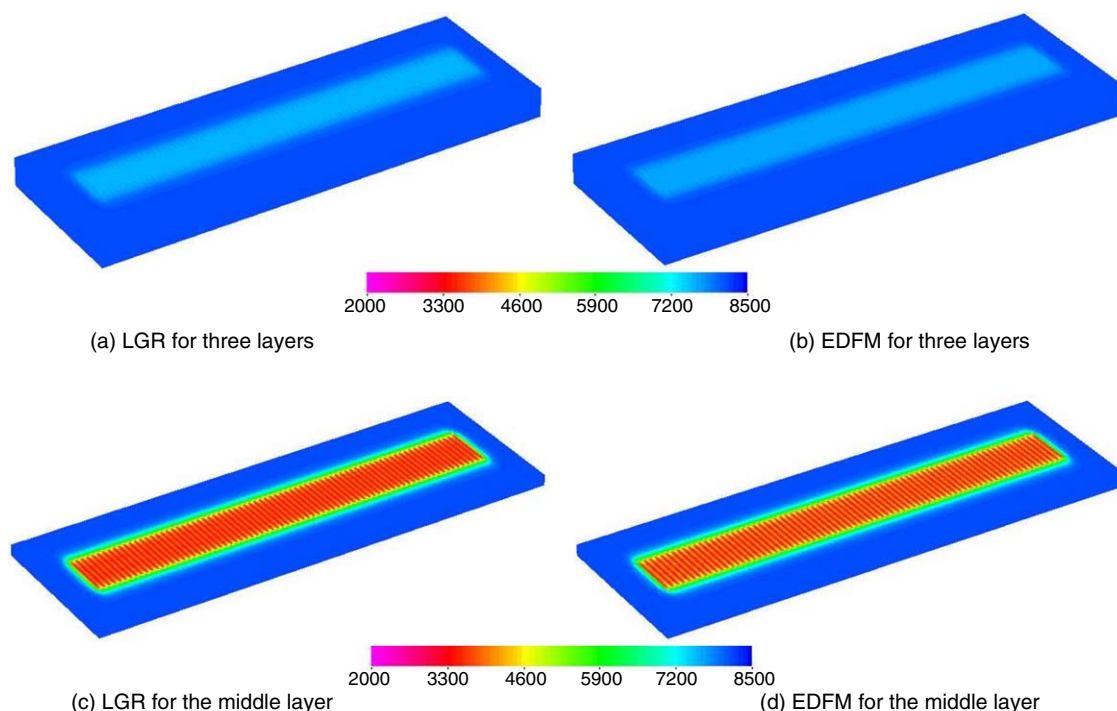


Fig. 7—Comparison of pressure distribution at the end of the simulation between LGR and EDFM.

In order to compare the CO₂ huff 'n' puff effectiveness, a base case with only primary production after the history-matching period under the condition of a minimum BHP of 2,000 psi was simulated. Fig. 8 shows the effects of different CO₂ diffusion coefficients on cumulative oil production. It can be seen that two cases with small CO₂ diffusion coefficients of 0.00001 and 0.0001 cm²/s underperformed the base case with primary production. The other two cases with large CO₂ diffusion coefficients of 0.001 and 0.01 cm²/s performed better than the base case with primary production at the end of simulation. The contribution to cumulative oil production after 7,300 days was approximately 3 and 9% for the two cases with CO₂ diffusion coefficients of 0.001 and 0.01 cm²/s, respectively. Accordingly, the effect of CO₂ molecular diffusion was very important when evaluating the CO₂ huff 'n' puff effectiveness in tight oil reservoirs. The expected CO₂ diffusion coefficient was approximately 0.001 cm²/s in this case study. It was strongly suggested that accurate measurements of CO₂ diffusion coefficients in the Eagle Ford tight oil reservoirs be considered.

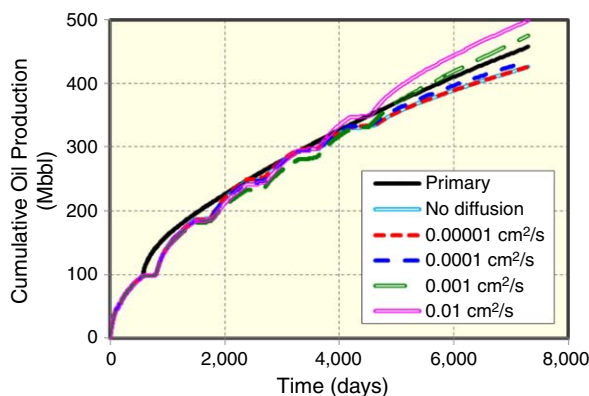


Fig. 8—Effects of different CO₂ diffusion coefficients on CO₂ huff 'n' puff effectiveness.

The effects of different CO₂ diffusion coefficients on cumulative CO₂ backflow are shown in Fig. 9. It clearly illustrates that a larger amount of CO₂ will backflow with a smaller CO₂ diffusion coefficient. The simulation results showed that approximately 87% of the injected CO₂ was produced back after 7,300 days with a small CO₂ diffusion coefficient of 0.00001 cm²/s, while 59% of the injected CO₂ was produced back with a large CO₂ diffusion coefficient of 0.01 cm²/s. The comparison of CO₂ gas mole fraction distribution after the fifth cycle of CO₂ soaking of CO₂ huff 'n' puff between cases of 0.00001 cm²/s and 0.01 cm²/s is shown in Fig. 10. It was observed that more CO₂ molecules diffused into the matrix with the larger CO₂ diffusion coefficient of 0.01 cm²/s. As a result, a better mixture of oil phase and CO₂ molecules resulted in a higher cumulative oil production.

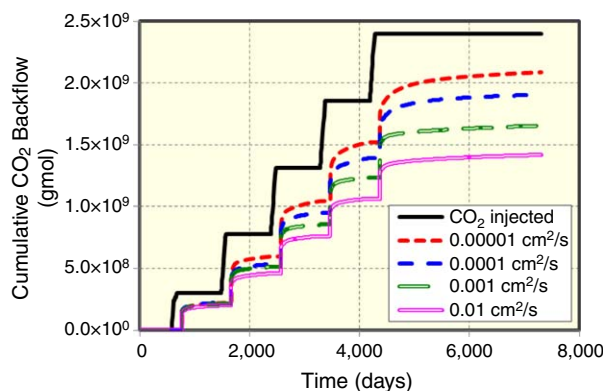


Fig. 9—Effects of different CO₂ diffusion coefficients on cumulative CO₂ backflow.

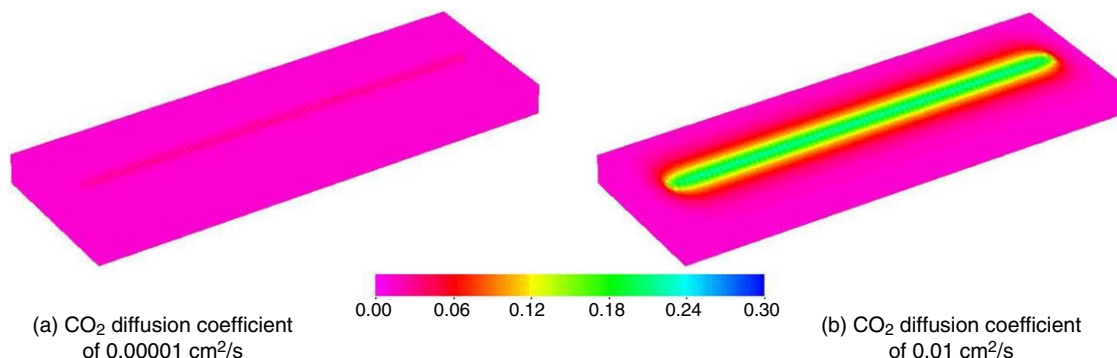


Fig. 10—Comparison of CO₂ gas mole fraction distribution after CO₂ soaking of the fifth cycle of CO₂ huff 'n' puff: (a) CO₂ diffusion coefficient of 0.00001 cm²/s, (b) CO₂ diffusion coefficient of 0.01 cm²/s.

The effects of different CO₂ diffusion coefficients on average reservoir pressure are presented in Fig. 11. As shown, average reservoir pressure increased with the increasing CO₂ diffusion coefficient. After 7,300 days of production, the difference in average reservoir pressure between the case with the CO₂ diffusion coefficient of 0.01 cm²/s and the base case with primary production was approximately 812 psi, leading to increased oil production. Fig. 12 displays the difference of pressure distribution between these two cases after 7,300 days of production. As shown, the average pressure of the case with CO₂ huff 'n' puff was larger than that of the base case, allowing the pressurized CO₂ to seep from hydraulic fractures into the tight rock.

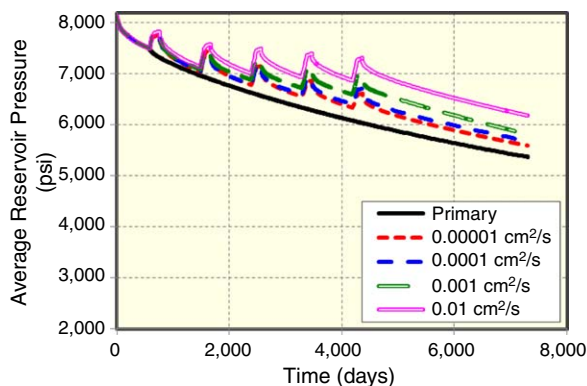


Fig. 11—Effects of different CO₂ diffusion coefficients on average reservoir pressure.

Effect of Nanopore Confinement. Pore-size distribution and surface-area analyses were performed on all the samples using an Autosorb-iQ-MP instrument (Quantachrome Instruments) equipped with a vacuum pump capable of reaching 5×10^{-7} Pa. Samples were pulverized into 100-mesh-size powder and were removed as soluble organic matter with CH₂Cl₂ extraction, and approximately 100-mg solvent-extracted samples were placed into 6-mm-stem quartz sample cells and degassed for 8 hours at 250°C under vacuum. Nitrogen at 77 K was used as the probe gas for all the experiments. Surface areas were calculated using a linear range between 0.05 and 0.3 P/P₀ of N₂ sorption, with a minimum of five points used in the Brunauer-Emmett-Teller (BET) surface-area analysis. Pore-size distribution was obtained using both the density functional theory (DFT) method and the Barrett-Joyner-Halenda (BJH) method. Because the BJH calculation could not give a realistic description of the filling of micropores (<2 nm in width) and narrow mesopores (2–50 nm), this often resulted in an underestimation of pore size. In order to achieve more-realistic values, we used DFT simulations for micropores and mesopores, and the BJH method for macropores (>50 nm in width). The combination of BJH and DFT methods determined pore sizes from <2 nm to 300 nm in the pore-width range.

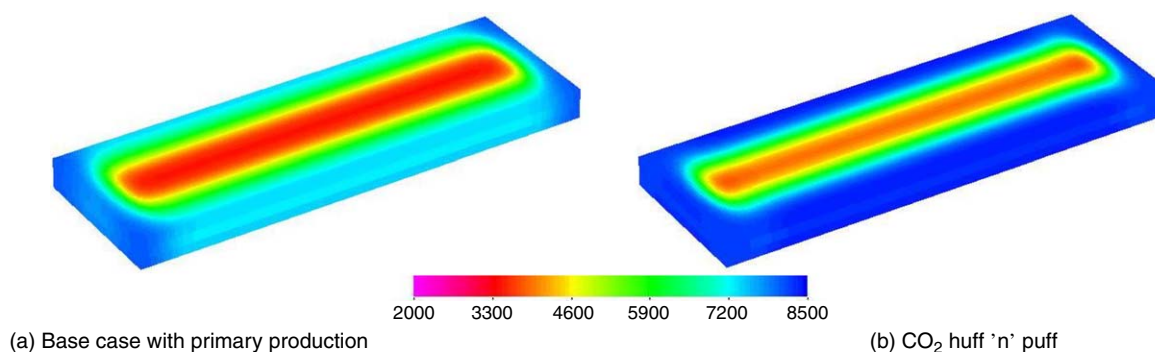


Fig. 12—Comparison of pressure distribution after 7,300 days between primary production and CO₂ huff 'n' puff with a CO₂ diffusion coefficient of 0.01 cm²/s: (a) base case with primary production, (b) CO₂ huff 'n' puff.

The organic-rich marl, which was one of the key lithofacies in the lower Eagle Ford Formation, contained a total-organic-carbon (TOC) content of 4.2%, and its measured global reporting initiative (GRI) helium porosity was 12.4%, after oil removal with CH₂Cl₂. The measured BET surface area was 19.6 m²/g rock, and the average pore size was 9 nm. The nanopore size distribution is shown in **Fig. 13**. For oil-bearing samples, the pore volume (PV) significantly increased after removing the residual oil by solvent extraction, showing that oil was mainly stored in pores with widths larger than 5 nm. The contribution of <5, 5–10, 10–20, 20–40, and >40 nm pores to the total porosity was 42, 27, 13, 4, and 14%, respectively. In addition, the pores that measured smaller than 10 nm took up almost 80% of the total porosity; therefore, nanopore confinement was needed in our modeling and a pore size of 10 nm was assigned in the following simulation study.

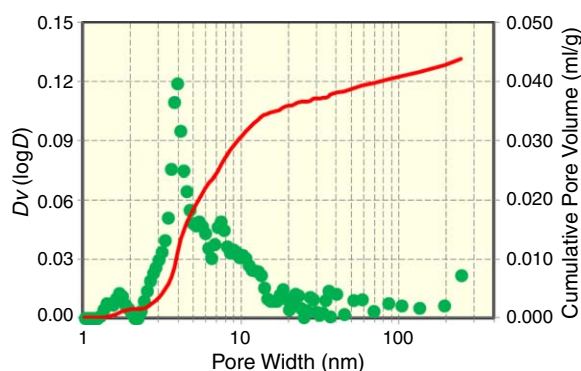


Fig. 13—Pore-size distribution of organic-rich marl in lower Eagle Ford Formation.

Thermal maturity also played an important role in organic-matter-hosted nanopore development and the variation of oil and gas chemical properties (Zhang et al. 2017a). With an increase of thermal maturity, pores with widths <10 nm increased and pores with widths greater than 40 nm were diminished (Milliken et al. 2013; Ko et al. 2017). The development of smaller pores was associated with high thermal maturity, and the reduction of larger pores possibly resulted from burial-related compaction and cementation. Thermal maturity greatly affected pore-size distribution, in particular for pores with widths <10 nm. Integrated studies that include scanning-electron-microscope (SEM) pore imaging were required to adequately define the genetic relationships among pore sizes, pore types, mineralogy, and rock texture. As shown in **Fig. 14**, the size of organic-matter-hosted pores ranged from a few nanometers to a few hundred nanometers.

The nanopore size significantly affected the critical properties of different components. **Table 4** compares the difference in critical temperature and pressure of six components between 10 nm, 20 nm, and bulk pore size. It can be clearly seen that both critical temperature and critical pressure decreased when the pore size decreased. In the following CO₂ huff 'n' puff simulation, the pressure/volume/temperature (PVT) data corresponding to 10 nm of pore size was updated and utilized. The impacts of different pore sizes and pore size distribution on the CO₂ huff 'n' puff effectiveness will be examined in a future study. **Fig. 15** shows the bubblepoint pressure under different pore sizes. The nanopore confinement led to suppression of the bubblepoint pressure; hence, the smaller the pore size, the larger the reduction.

The effects of CO₂ molecular diffusion and nanopore confinement on CO₂ huff 'n' puff effectiveness are shown in **Fig. 16**. The maximum value of CO₂ diffusion coefficient of 0.01 cm²/s was considered in this study. It should be mentioned that a more realistic value of diffusion coefficient needs future experimental measurements to determine, which is beyond the scope of this study. As can be seen, the contribution to cumulative oil production after 7,300 days was approximately 12% when compared with the primary production with the new PVT properties. It was measured at larger than 9% when only the effect of CO₂ molecular diffusion was considered. Hence, an accurate modeling of the CO₂ huff 'n' puff process is necessary when considering the effect of nanopore confinement. The effect of CO₂ huff 'n' puff on average reservoir pressure with consideration given to CO₂ molecular diffusion and nanopore confinement is presented in **Fig. 17**. After 7,300 days of production, the difference in average reservoir pressure between the case with CO₂ huff 'n' puff and the base case with primary production was approximately 779 psi. **Fig. 18** displays the difference in pressure distribution between these two cases after 7,300 days of production, illustrating that the average pressure of the case with CO₂ huff 'n' puff was larger than that of the base case.

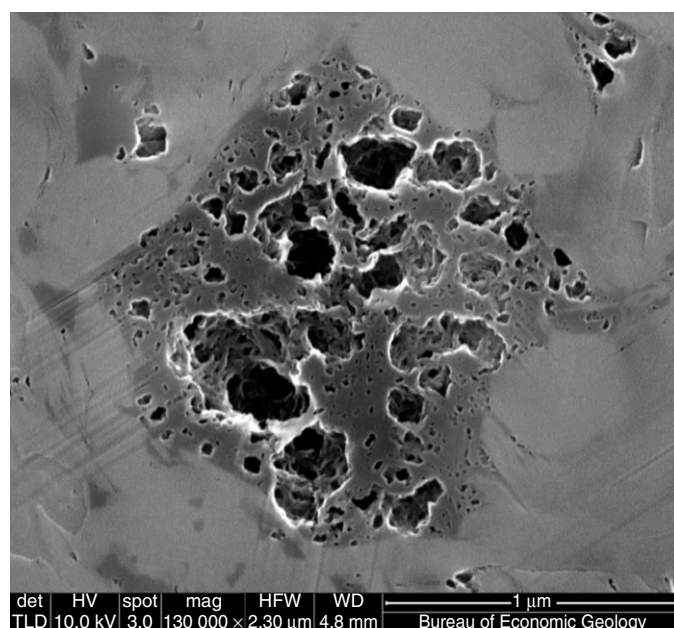


Fig. 14—SEM pore image of organic-rich marl in lower Eagle Ford Formation.

Component	Critical Temperature (K)			Critical Pressure (atm)		
	10 nm	20 nm	Bulk	10 nm	20 nm	Bulk
CO ₂	293.06	298.6	304.20	70.1	71.5	72.8
N ₂	121.74	123.96	126.20	32.3	32.9	33.5
C ₁	183.61	187.09	190.60	43.7	44.6	45.4
C ₂ –C ₅	262.53	268.6	274.74	34.9	35.7	36.5
C ₆ –C ₁₀	412.97	425.72	438.68	23.6	24.4	25.1
C ₁₁₊	682.36	711.00	740.29	16.1	16.8	17.5

Table 4—Effect of pore size on the critical temperature and critical pressure of six components.

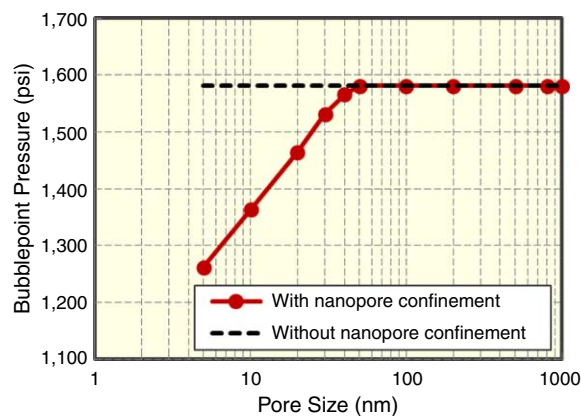


Fig. 15—Bubblepoint pressure under different pore sizes.

Effect of Complex Natural Fractures. In addition to 76 hydraulic fractures, a total of 1,800 natural fractures was assumed in the reservoir volume studied, assuming each layer contained 600 natural fractures, as shown in Fig. 19a. Fig. 19b displays a small portion of the third layer with multiple hydraulic fractures shown in blue and natural fractures shown in black. As shown, the complex fracture geometry was exactly captured through the EDFM method. In this study, we used a statistical method to generate the two sets of natural fractures. The angle, with respect to the x -axis, for one set ranged from 0 to 20° and the other set ranged from 90 to 110°. The length of natural fractures varied between 100 and 300 ft. The conductivity of the natural fractures was given by 10 md-ft. It was assumed that the height of natural fractures in each layer was equal to the reservoir thickness of the corresponding layer. The reason for generating such natural-fracture geometry was so that a more connected fracture network could be formed. It is also important to mention that the above history-matching process was not performed separately with the same natural fractures considered to obtain history-matched

variables to be used as input for the prediction simulations because of the highly uncertain distribution of natural fractures and less available information. The effect of the uncertainty in natural-fracture properties, such as orientation, density, length, height, aperture, and permeability, on history matching and CO₂ huff 'n' puff effectiveness will be examined in more detail in a future study.

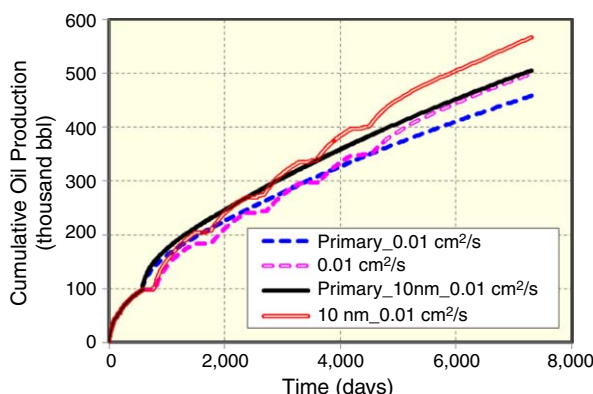


Fig. 16—Effect of CO₂ huff 'n' puff on cumulative oil production considering CO₂ molecular diffusion and nanopore confinement.

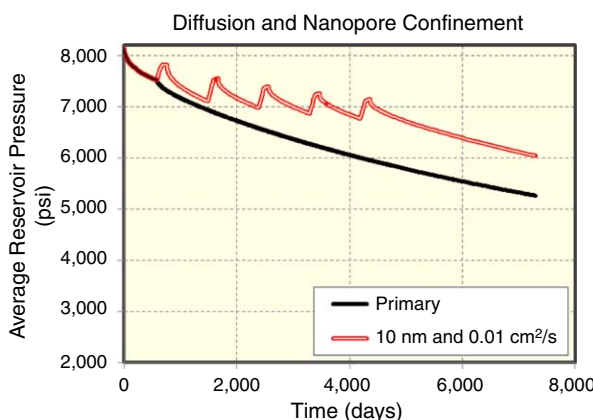


Fig. 17—Effect of CO₂ huff 'n' puff on average reservoir pressure considering CO₂ molecular diffusion and nanopore confinement.

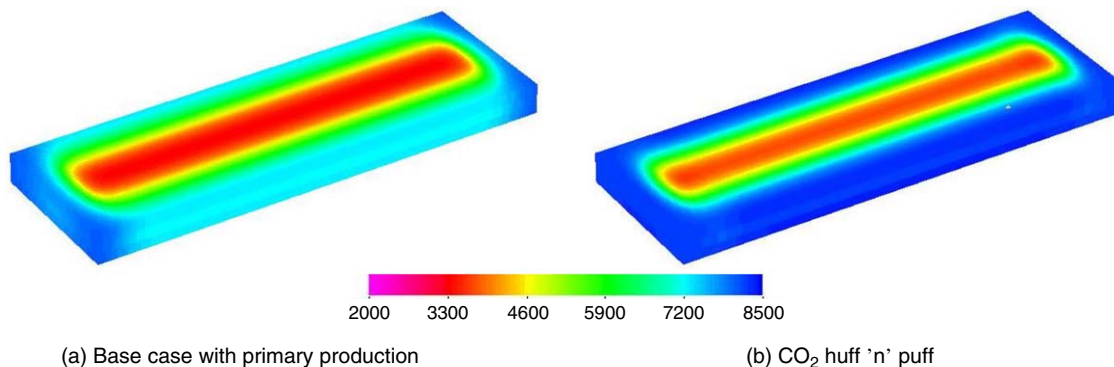
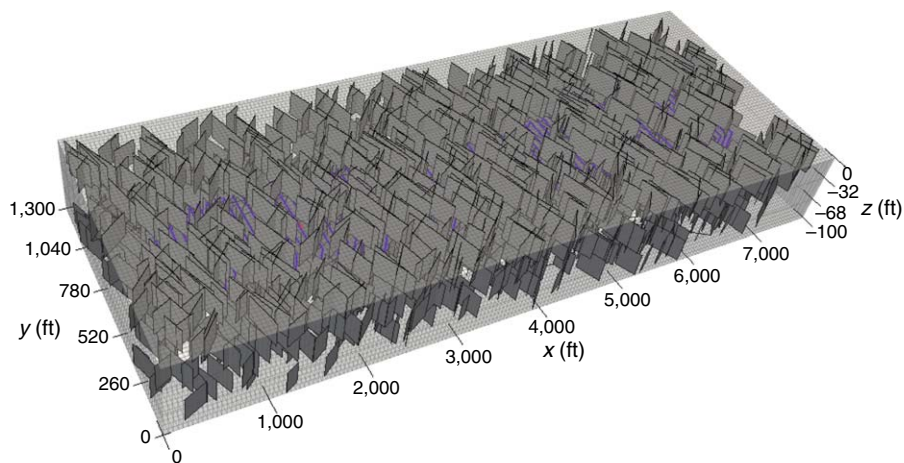
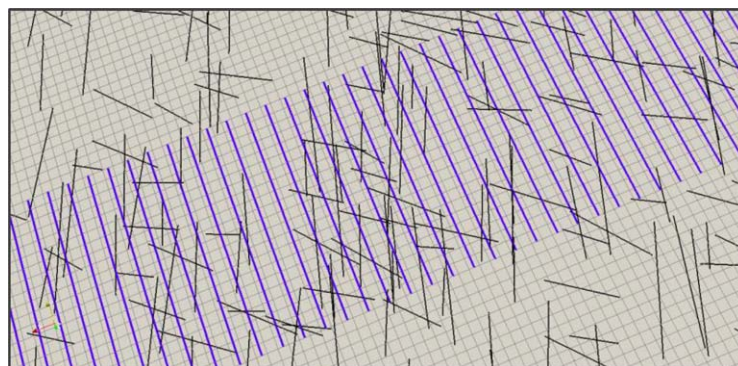


Fig. 18—Comparison of pressure distribution after 7,300 days between primary production and CO₂ huff 'n' puff with a CO₂ diffusion coefficient of 0.01 cm²/s and 10-nm nanopore size.

A CO₂ diffusion coefficient of 0.01 cm²/s and 10-nm pore size were used in the simulation. The effect of CO₂ huff 'n' puff on well performance considering complex natural fractures is shown in Fig. 20. As shown, the contribution to cumulative oil production after 7,300 days was approximately 8% when compared to the primary production with complex natural fractures. The effect of CO₂ huff 'n' puff on average reservoir pressure considering complex natural fractures is presented in Fig. 21. After 7,300 days of production, the difference in average reservoir pressure between the case with CO₂ huff 'n' puff and the base case with primary production was approximately 625 psi. Fig. 22 displays the difference in pressure distribution of the three layers, as well as the middle layer between these two cases, after 7,300 days of production. The average pressure of the case with CO₂ huff 'n' puff was larger than that of the base case. The CO₂-gas-mole-fraction distribution after soaking the fifth cycle of CO₂ huff 'n' puff with complex natural fractures is shown in Fig. 23, clearly illustrating the effective penetration area of CO₂ molecules into the tight rock matrix. An asymmetric CO₂ molecule distribution was formed because of the interaction between hydraulic fractures and complex natural fractures.



(a) A three-layer reservoir model with multiple hydraulic and natural fractures



(b) A small portion of the third-layer model with multiple hydraulic and natural fractures

Fig. 19—A 3D reservoir model with a horizontal well and 76 biwing hydraulic fractures and 1,800 natural fractures.

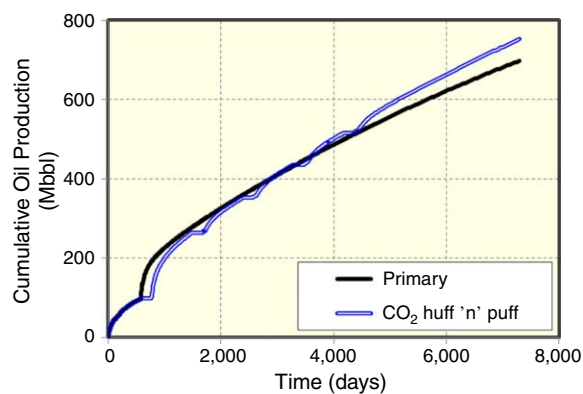


Fig. 20—Effect of CO₂ huff 'n' puff on cumulative oil production considering complex natural fractures.

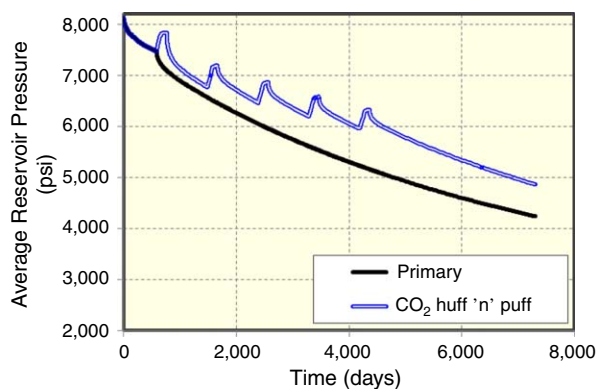


Fig. 21—Effect of CO₂ huff 'n' puff on average reservoir pressure considering complex natural fractures.

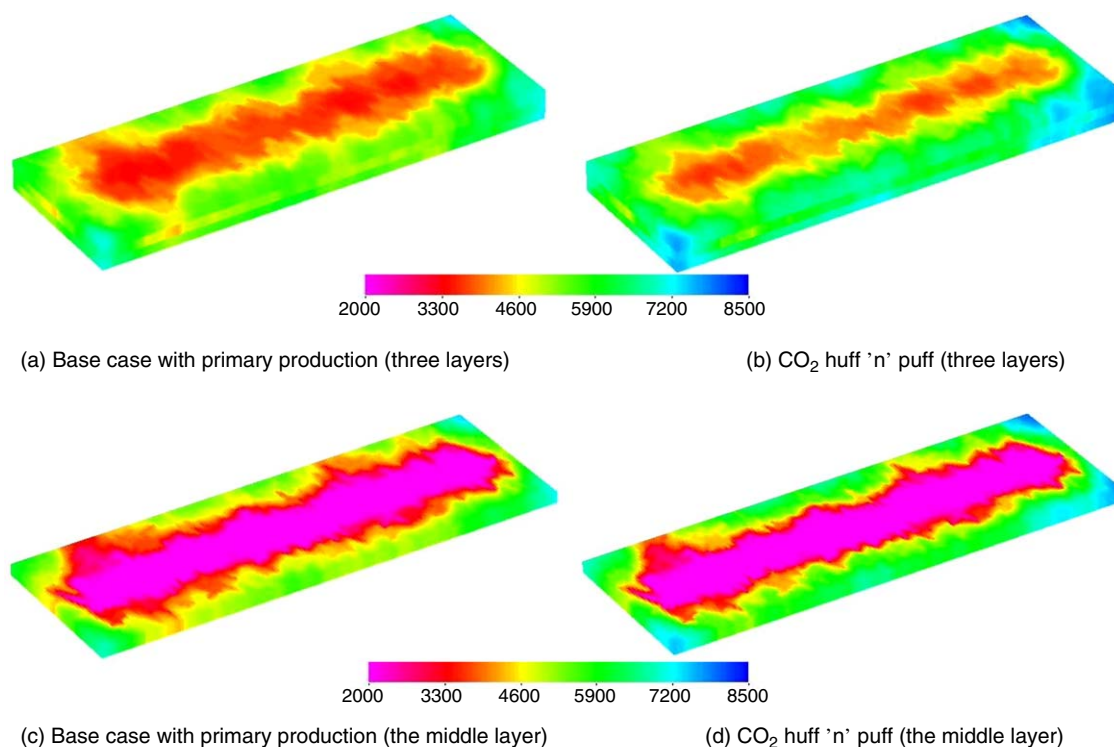


Fig. 22—Comparison of pressure distribution after 7,300 days between primary production and CO₂ huff 'n' puff with complex natural fractures.

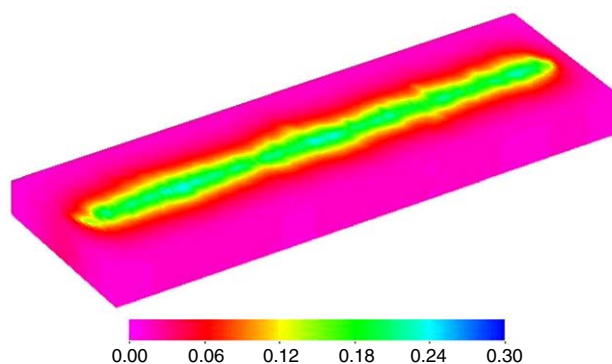


Fig. 23—CO₂-gas-mole-fraction distribution after CO₂ soaking of the fifth cycle of CO₂ huff 'n' puff with complex natural fractures.

Conclusions

We introduced a numerical compositional model in combination with the EDFM method to simulate CO₂ huff 'n' puff in a tight oil reservoir with complex fracture geometries. The physical mechanisms of CO₂ molecular diffusion and nanopore confinement were accurately captured. The compositional model was validated through history matching with an actual Eagle Ford tight oil well. The effects of CO₂ molecular diffusion and nanopore confinement and complex natural fractures on the CO₂ huff 'n' puff effectiveness were examined. The following conclusions were drawn from the study:

1. The EDFM method was faster and easier than the traditional LGR method for simulating multiphase flow in tight oil reservoirs with complex fracture geometries.
2. Both CO₂ molecular diffusion and nanopore confinement were important physical mechanisms for accurately evaluating CO₂ huff 'n' puff effectiveness in tight oil reservoirs. Both mechanisms had positive effects on the CO₂ huff 'n' puff effectiveness.
3. The CO₂ huff 'n' puff with the smaller CO₂ diffusion coefficients measured at 0.00001 to 0.0001 cm²/s underperformed the primary production, while it performed better than the primary production with larger CO₂ diffusion coefficients measured at 0.001 to 0.01 cm²/s.
4. The contribution of CO₂ huff 'n' puff to cumulative oil production after 7,300 days with a CO₂ diffusion coefficient of 0.01 cm²/s and nanopore size of 10 nm was approximately 12% for the actual Eagle Ford tight oil well investigated in this study.
5. The presence of natural fractures significantly affected primary production and CO₂ huff 'n' puff effectiveness in the tight oil reservoir. The contribution of CO₂ huff 'n' puff to cumulative oil production after 7,300 days with complex natural fractures (CO₂ diffusion coefficient of 0.01 cm²/s and nanopore size of 10 nm were still considered) was approximately 8% for this actual Eagle Ford tight oil well.
6. This study provided a better numerical tool for effectively and efficiently simulating a CO₂ huff 'n' puff process in tight oil reservoirs with complex fracture geometries and complex nanopore mechanisms.

Nomenclature

- a = parameter calculated using van der Waals mixing rules
 b = parameter calculated using van der Waals mixing rules
 A_{NNC} = contact area between the NNC pair
 d_{NNC} = distance between the NNC pair
 f_L^i = fugacity of component i in the liquid phase
 f_V^i = fugacity of component i in the vapor phase
 F = number of moles of original fluid feed
 k_f = fracture permeability
 k_{NNC} = permeability associated with the connection
 L = number of moles of liquid phase
 L_{fs} = fracture-segment length
 N_c = number of components
 P_{cap} = capillary pressure
 P_{cb} = bulk critical pressure
 P_{cp} = pore critical pressure
 $[P]_i$ = parachor of component i in the liquid or gas phase
 P_L = pressures in the liquid phase
 P_V = pressures in the vapor phase
 r_p = pore-throat radius
 R = universal gas constant
 T = reservoir temperature
 T_{cb} = bulk critical temperature
 T_{cp} = pore critical temperature
 V = number of moles of vapor phase
 V_m = mole volume of component i
 w_f = fracture width
 W_{fs} = fracture-segment height
 x_i = mole fractions of component i in the liquid phase
 y_i = mole fractions of component i in the vapor phase
 z_i = overall mole fraction of component i
 ΔT_c^* = relative critical temperature shift
 ΔP_c^* = relative critical pressure shift
 θ = contact angle
 $\bar{\rho}_L$ = density of the bulk liquid phase
 $\bar{\rho}_V$ = density of the bulk vapor phase
 σ = interfacial tension
 σ_{LJ} = Lennard-Jones size parameter
 v = scaling exponent

Acknowledgments

The authors would like to acknowledge financial support from the National Natural Science Foundation of China (Grant No. 51728401). We would also like to acknowledge the Computer Modelling Group for providing the CMG-GEM software for this study.

References

- Adamson, A. W. 1990. *Physical Chemistry of Surfaces*, fifth edition. New York City: John Wiley & Sons.
 Adekunle, O. and Hoffman, B. T. 2014. Minimum Miscibility Pressure Studies in the Bakken. Presented at the SPE Improved Oil Recovery Symposium, Tulsa, Oklahoma, 12–16 April. SPE-169077-MS. <https://doi.org/10.2118/169077-MS>.
 Brusilovsky, A. I. 1992. Mathematical Simulation of Phase Behavior of Natural Multicomponent Systems at High Pressures With an Equation of State. *SPE Res Eval & Eng* 7 (1): 117–22. SPE-20180-PA. <https://doi.org/10.2118/20180-PA>.
 Chen, C., Balhoff, M., and Mohanty, K. K. 2014. Effect of Reservoir Heterogeneity on Primary Recovery and CO₂ Huff ‘n’ Puff Recovery in Shale-Oil Reservoirs. *SPE Res Eval & Eng* 17 (3): 404–413. SPE-164553-PA. <https://doi.org/10.2118/164553-PA>.
 Cipolla, C. L. and Wallace, J. 2014. Stimulated Reservoir Volume: A Misapplied Concept? Presented at the SPE Hydraulic Fracturing Technology Conference, The Woodlands, Texas, 4–6 February. SPE-168596-MS. <https://doi.org/10.2118/168596-MS>.
 CMG-GEM. 2016. *GEM User's Guide*. Calgary, Alberta, Canada: Modeling Group Ltd.
 de Araujo Cavalcante Filho, J. S., Shakiba M., Moinfar A. et al. 2015. Implementation of a Preprocessor for Embedded Discrete Fracture Modeling in an IMPEC Compositional Reservoir Simulator. Presented at the SPE Reservoir Simulation Symposium, Houston, Texas, 23–25 February. SPE-173289-MS. <https://doi.org/10.2118/173289-MS>.
 Devogowda, D., Sapmanee, K., Civan, F. et al. 2012. Phase Behavior of Gas Condensates in Shales Due to Pore Proximity Effects: Implications for Transport, Reserves and Well Productivity. Presented at the SPE Annual Technical Conference and Exhibition, San Antonio, Texas, 8–10 October. SPE-160099-MS. <https://doi.org/10.2118/160099-MS>.
 Diaz Campos, M., Akkutlu, I. Y., and Sigal, R. F. 2009. A Molecular Dynamics Study on Natural Gas Solubility Enhancement in Water Confined to Small Pores. Presented at the SPE Annual Technical Conference and Exhibition, New Orleans, Louisiana, 4–7 October. SPE-124491-MS. <https://doi.org/10.2118/124491-MS>.
 Grogan, A. T., Pinczewski, V. W., Ruskau, G. J. et al. 1988. Diffusion of CO₂ at Reservoir Conditions: Models and Measurements. *SPE Res Eval & Eng* 3 (1): 93–102. SPE-14897-PA. <https://doi.org/10.2118/14897-PA>.
 Hawthorne, S. B., Gorecki, C. D., Sorensen, J. A. et al. 2013. Hydrocarbon Mobilization Mechanisms From Upper, Middle, and Lower Bakken Reservoir Rocks Exposed to CO₂. Presented at the SPE Unconventional Resources Conference, Calgary, Canada, 5–7 November. SPE-167200-MS. <https://doi.org/10.2118/167200-MS>.

- Hoteit, H. and Firoozabadi, A. 2006. Compositional Modeling by the Combined Discontinuous Galerkin and Mixed Method. *SPE J.* **11** (1): 19–34. SPE-90276-PA. <https://doi.org/10.2118/90276-PA>.
- Hoteit, H. 2013. Modeling Diffusion and Gas-Oil Mass Transfer in Fractured Reservoirs. *J Pet Sci Eng* **105**: 1–17. <https://doi.org/10.1016/j.petrol.2013.03.007>.
- Hui, M. H., Mallison, B. T., Fyrozjaee, M. H. et al. 2013. The Upscaling of Discrete Fracture Models for Faster, Coarse-Scale Simulations of IOR and EOR Processes for Fractured Reservoirs. Presented at the SPE Annual Technical Conference and Exhibition, New Orleans, Louisiana, 30 September–2 October. SPE-166075-MS. <https://doi.org/10.2118/166075-MS>.
- Ko, L., Loucks, R. G., Ruppel, S. C. et al. 2017. Origin and Characterization of Eagle Ford Pore Networks in the South Texas Upper Cretaceous Shelf. *AAPG Bull* **101** (3): 387–418. <https://doi.org/10.1306/08051616035>.
- Kumar, P. and Mittal, K. L. (eds.). 1999. *Handbook of Microemulsion Science and Technology*. New York: Marcel Dekker.
- Kurtoglu, B., Sorensen, J. A., Braunberger, J. et al. 2013. Geologic Characterization of a Bakken Reservoir for Potential CO₂ EOR. Presented at the Unconventional Resources Technology Conference, Denver, Colorado, 12–14 August. URTEC-1619698-MS. <https://doi.org/10.15530/URTEC-1619698-MS>.
- Li, L. and Lee, S. H. 2008. Efficient Field-Scale Simulation of Black Oil in a Naturally Fractured Reservoir Through Discrete Fracture Networks and Homogenized Media. *SPE Res Eval & Eng* **11** (4): 750–758. SPE-103901-PA. <https://doi.org/10.2118/103901-PA>.
- Milliken, K. L., Rudnicki, M., Awwiller, D. N. et al. 2013. Organic Matter-Hosted Pore System, Marcellus Formation (Devonian), Pennsylvania. *AAPG Bull* **97** (2): 177–200. <https://doi.org/10.1306/07231212048>.
- Mirzaei, M. and Cipolla, C. L. 2012. A Workflow for Modeling and Simulation of Hydraulic Fractures in Unconventional Gas Reservoirs. Presented at the SPE Middle East Unconventional Gas Conference and Exhibition, Abu Dhabi, UAE, 23–25 January. SPE-153022-MS. <https://doi.org/10.2118/153022-MS>.
- Moinfar, A., Varavei, A., Sepehrnoori, K. et al. 2014. Development of an Efficient Embedded Discrete Fracture Model for 3D Compositional Reservoir Simulation in Fractured Reservoirs. *SPE J.* **19** (2): 289–303. SPE-154246-PA. <https://doi.org/10.2118/154246-PA>.
- Nojabaei, B., Siripatrachai, N., Johns, R. T. et al. 2014. Effect of Saturation Dependent Capillary Pressure on Production in Tight Rocks and Shales: A Compositionally Extended Black Oil Formulation. Presented at the SPE Eastern Regional Meeting, Charleston, West Virginia, 21–23 October. SPE-171028-MS. <https://doi.org/10.2118/171028-MS>.
- Pedersen, K. S. and Christensen, P. L. 2007. *Phase Behavior of Petroleum Reservoir Fluids*. Boca Raton, Florida: CRC/Taylor & Francis.
- Peng, D. Y. and Robinson, D. B. 1976. A New Two-Constant Equation of State. *Ind. Eng. Chem. Fundamen.* **15** (1): 59–64. <https://doi.org/10.1021/il60057a011>.
- Rachford, H. H. and Rice, J. D. 1952. Procedure for Use of Electronic Digital Computers in Calculating Flash Vaporization Hydrocarbon Equilibrium. *J Pet Technol* **4** (10): 19–20. SPE-952327-G. <https://doi.org/10.2118/952327-G>.
- Reid, R. C., Prausnitz, J. M., and Poling, B. E. 1987. *The Properties of Gases and Liquids*. New York: McGraw Hill.
- Ren, B., Xu, Y., Niu, B. et al. 2011. Laboratory Assessment and Field Pilot of Near Miscible CO₂ Injection for IOR and Storage in a Tight Oil Reservoir of Shengli Oilfield China. Presented at the SPE Enhanced Oil Recovery Conference, Kuala Lumpur, Malaysia, 19–21 July. SPE-144108-MS. <https://doi.org/10.2118/144108-MS>.
- Renner, T. A. 1988. Measurement and Correlation of Diffusion Coefficients for CO₂ and Rich-Gas Applications. *SPE Res Eval & Eng* **3** (2): 517–523. SPE-15391-PA. <https://doi.org/10.2118/15391-PA>.
- Rezaveisi, M., Sepehrnoori, K., and Pope, G. A. 2015. Compositional Simulation Including Effect of Capillary Pressure on Phase Behavior. Presented at the SPE Annual Technical Conference and Exhibition, Houston, Texas, 28–30 September. SPE-175135-MS. <https://doi.org/10.2118/175135-MS>.
- Sandoval, D., Yan, W., Michelsen, M. L. et al. 2015. Phase Envelope Calculations for Reservoir Fluids in the Presence of Capillary Pressure. Presented at SPE Annual Technical Conference and Exhibition, Houston, Texas, 28–30 September. SPE-175110-MS. <https://doi.org/10.2118/175110-MS>.
- Sandve, T. H., Berre, I., and Nordbotten, J. M. 2012. An Efficient Multi-Point Flux Approximation Method for Discrete Fracture–Matrix Simulations. *J Comput Phys* **231** (9): 3784–3800. <https://doi.org/10.1016/j.jcp.2012.01.023>.
- Shakiba, M. and Sepehrnoori, K. 2015. Using Embedded Discrete Fracture Model (EDFM) and Microseismic Monitoring Data to Characterize the Complex Hydraulic Fracture Networks. Presented at the SPE Annual Technical Conference and Exhibition, Houston, Texas, 28–30 September. SPE-175142-MS. <https://doi.org/10.2118/175142-MS>.
- Shoaib, S. and Hoffman, B. T. 2009. CO₂ Flooding of the Elm Coulee Field. Presented at the SPE Rocky Mountain Petroleum Technology Conference, Denver, Colorado, 14–16 April. SPE-123176-MS. <https://doi.org/10.2118/123176-MS>.
- Simpson, M. D., Patterson, R., and Wu, K. 2016. Study of Stress Shadow Effects in Eagle Ford Shale: Insight From Field Data Analysis. Presented at the 50th US Rock Mechanics/Geomechanics Symposium, Houston, Texas, 26–29 June. ARMA-2016-190.
- Song, C. and Yang, D. 2013. Performance Evaluation of CO₂ Huff ‘n’ Puff Processes in Tight Oil Formations. Presented at the SPE Unconventional Resources Conference, Alberta, Canada, 5–7 November. SPE-167217-MS. <https://doi.org/10.2118/167217-MS>.
- Wang, X., Luo, P., Er, V. et al. 2010. Assessment of CO₂ Flooding Potential for Bakken Formation, Saskatchewan. Presented at the Canadian Unconventional Resources and International Petroleum Conference, Calgary, Canada, 19–21 October. SPE-137728-MS. <https://doi.org/10.2118/137728-MS>.
- Wu, K. and Olson, J. E. 2016. Numerical Investigation of Complex Fracture Networks in Naturally Fractured Reservoirs. *SPE Prod & Oper* **31** (4): 300–309. SPE-173326-PA. <https://doi.org/10.2118/173326-PA>.
- Wu, R., Kresse, O., Weng, X. et al. 2012. Modeling of Interaction of Hydraulic Fractures in Complex Fracture Networks. Presented at the SPE Hydraulic Fracture Technology Conference, The Woodlands, Texas, 6–8 February. SPE-152052-MS. <https://doi.org/10.2118/152052-MS>.
- Xu, Y. 2015. *Implementation and Application of the Embedded Discrete Fracture Model (EDFM) for Reservoir Simulation in Fractured Reservoirs*. MS thesis, The University of Texas at Austin, Austin, Texas (December 2015).
- Xu, Y., Cavalcante Filho, J. S. A., Yu, W. et al. 2017a. Discrete-Fracture Modeling of Complex Hydraulic-Fracture Geometries in Reservoir Simulators. *SPE Res Eval & Eng* **20** (2): 403–422. SPE-183647-PA. <https://doi.org/10.2118/183647-PA>.
- Xu, Y., Yu, W., and Sepehrnoori, K. 2017b. Modeling Dynamic Behaviors of Complex Fractures in Conventional Reservoir Simulators. Presented at the SPE/AAPG/SEG Unconventional Resources Technology Conference, Austin, Texas, 24–26 July. URTEC-2670513-MS. <https://doi.org/10.15530/URTEC-2017-2670513>.
- Yu, W., Lashgari, H. R., and Sepehrnoori, K. 2014. Simulation Study of CO₂ Huff ‘n’ Puff Process in Bakken Tight Oil Reservoirs. Presented at the SPE Western North American and Rocky Mountain Joint Meeting, Denver, Colorado, 17–18 April. SPE-169575-MS. <https://doi.org/10.2118/169575-MS>.
- Yu, W., Lashgari, H. R., Wu, K. et al. 2015. CO₂ Injection for Enhanced Oil Recovery in Bakken Tight Oil Reservoirs. *Fuel* **159**: 354–363. <https://doi.org/10.1016/j.fuel.2015.06.092>.
- Yu, W., Xu, Y., Weijermars, R. et al. 2018. A Numerical Model for Simulating Pressure Response of Well Interference and Well Performance in Tight Oil Reservoirs With Complex-Fracture Geometries Using the Fast Embedded-Discrete-Fracture-Model Method. *SPE Res Eval & Eng* **21** (2): 489–502. SPE-184825-PA. <https://doi.org/10.2118/184825-PA>.

- Zhang, T., Sun, X., Milliken, K. et al. 2017a. Empirical Relationship Between Gas Composition and Thermal Maturity in Eagle Ford Shale, South Texas. *AAPG Bull* **101** (8): 1277–1307. <https://doi.org/10.1306/09221615209>.
- Zhang, Y., Lashgari, H. R., Di, Y. et al. 2016. Capillary Pressure Effect on Hydrocarbon Phase Behavior in Unconventional Reservoirs. Presented at the SPE Low Perm Symposium, Denver, Colorado, 5–6 May. SPE-180235-MS. <https://doi.org/10.2118/180235-MS>.
- Zhang, Y., Yu, W., Sepehrnoori, K. et al. 2017b. A Comprehensive Numerical Model for Simulating Fluid Transport in Nanopores. *Sci Rep* **7**: 40507. <https://doi.org/10.1038/srep40507>.
- Zhang, Y., Yu, W., Di, Y. et al. 2017c. Investigation of Nanopore Confinement on Fluid Flow in Tight Reservoirs. *J Pet Sci Eng* **150**: 265–271. <https://doi.org/10.1016/j.petrol.2016.11.005>.
- Zhang, Y., Di, Y., Yu, W. et al. 2017d. A Comprehensive Model for Investigation of CO₂-EOR With Nanopore Confinement in the Bakken Tight Oil Reservoir. Presented at the SPE Annual Technical Conference and Exhibition, San Antonio, Texas, 9–11 October. SPE-187211-PA. <https://doi.org/10.2118/187211-PA>.
- Zuloaga-Molero, P., Yu, W., Xu, Y. et al. 2016. Simulation Study of CO₂-EOR in Tight Oil Reservoirs With Complex Fracture Geometries. *Sci Rep* **6**: 33445. <https://doi.org/10.1038/srep33445>.

SI Metric Conversion Factors

ft × 3.048*	E-01 = m
ft ³ × 2.832	E-02 = m ³
cp × 1.0	E-03 = Pa·s
psi × 6.895	E+00 = kPa
md × 1e-15	E+00 = m ²

*Conversion factor is exact.

Wei Yu is currently a research associate in the Hildebrand Department of Petroleum and Geosystems Engineering, University of Texas at Austin, and a research associate in the Harold Vance Department of Petroleum Engineering, Texas A&M University. His research interests include EDFM technology, shale gas and tight oil reservoir simulation, unconventional EOR simulation, well-spacing optimization, automatic history matching, and data mining. Yu has authored or coauthored more than 100 technical papers, holds one patent, and has published one book (*Shale Gas and Tight Oil Reservoir Simulation*). He earned a BS degree in applied chemistry from the University of Jinan in China, an MS degree in chemical engineering from Tsinghua University in China, and a PhD degree in petroleum engineering from the University of Texas at Austin. Yu is an active member of SPE.

Yuan Zhang is a lecturer in the School of Energy Resources at China University of Geosciences, Beijing. Her research interests include phase behavior and gas EOR in unconventional reservoirs. Zhang has authored or coauthored more than 10 technical papers. She earned a BS degree in petroleum engineering from China University of Geosciences, Beijing and a PhD degree in energy and resources engineering from Peking University. Zhang is an active member of SPE.

Abdoljalil Varavei is a petroleum engineering consultant (senior reservoir engineer) and a research associate in the Center for Petroleum and Geosystems Engineering at the University of Texas at Austin. His expertise includes improved oil recovery and EOR, reservoir modeling and performance analysis for conventional and unconventional reservoirs, reservoir simulation, software development and application, and multiphase flow in porous media and wellbores. Varavei holds a PhD degree in petroleum engineering from the University of Texas at Austin.

Kamy Sepehrnoori is a professor in the Department of Petroleum and Geosystems Engineering at the University of Texas at Austin, where he holds the W. A. (Monty) Moncrief Centennial Chair in Petroleum Engineering. His research interests and teaching include computational methods, reservoir simulation, parallel computing, EOR modeling, naturally fractured reservoirs, and unconventional resources. Sepehrnoori is the director of the Reservoir Simulation Joint Industry Project in the Center for Petroleum and Geosystems Engineering. He holds a PhD degree from the University of Texas at Austin.

Tongwei Zhang is a research scientist and organic geochemist at the Bureau of Economic Geology at the University of Texas, Austin. He was a post-doctoral-degree scholar in chemistry at the California Institute of Technology, Pasadena, California. Zhang earned a BS degree in geology and a PhD degree in isotope geochemistry. His research focuses on gas and organic geochemistry, isotope geochemistry, gas adsorption in shale, and organic/inorganic interaction. Zhang is the director of the Organic Geochemistry Laboratory at the Bureau of Economic Geology.

Kan Wu is an assistant professor in the Harold Vance Department of Petroleum Engineering at Texas A&M University. Her research interests include hydraulic fracturing, coupled geomechanics/fluid-flow modeling, particle-laden flows, and optimization of well performance in unconventional reservoirs. Wu has authored or coauthored more than 50 technical papers. She holds a PhD degree in petroleum engineering from the University of Texas at Austin. Wu is a member of SPE.

Jijun Miao is the chief executive officer of Sim Tech and a research adviser in the Department of Petroleum and Geosystems Engineering at the University of Texas at Austin. His research interests include fracture characteristics, reservoir modeling and simulation, and EDFM development and application. Miao has authored or coauthored more than 35 technical papers and holds one patent. He holds a PhD degree in petroleum exploration from the Research Institute of Petroleum Exploration and Development, PetroChina. Miao has many years of hands-on oilfield experience in oil and gas exploration and development, and leads multidisciplinary research teams undertaking various research-and-development programs.